Shear-induced glass-to-crystal transition in anisotropic clay-like suspensions

Vincent Labalette, Alexis Praga, Florent Girard, Martine Meireles, Yannick Hallez, Jeffrey F Morris

Soft Matter

ARTICLE TYPE

Cite this: DOI: 00.0000/xxxxxxxxxx

Shear-induced glass-to-crystal transition in anisotropic clay-like suspensions†

Vincent Labalette,[ab] Alexis Praga,[ab] Florent Girard,[ab] Martine Meireles,[a] Yannick Hallez,[a] and Jeffrey F. Morris[c]

Received Date
Accepted Date

DOI: 00.0000/xxxxxxxxxx

A new numerical framework based on Stokesian dynamics is used to study a shear-induced glass-to-crystal transition in suspensions of clay-like anisotropically charged platelets. The structures obtained in quiescent conditions are in agreement with previous Monte Carlo results: a liquid phase at very short interaction range (high salt concentration), phase separation and a gel without large scale density fluctuations at intermediate interaction ranges, and glassy states at very large interaction ranges. When initially glassy suspensions are sheared, hydrodynamic torques first rotate platelets so they can reach a transient quasi-nematic disordered state. These orientational correlations permit to unlock translational degrees of freedom and the platelets then form strings aligned with the velocity direction and hexagonally packed in the gradient-vorticity plane. Under steady shear, platelet orientations are correlated but the system is not nematic. After flow cessation and relaxation in quiescent conditions, positional and orientational order are further improved as the platelet suspension experiences a transition to a nematic hexagonal crystal. Energy calculations and the existence of residual stress anisotropy after relaxation show that this final structure is not an equilibrium state but rather a new ordered, arrested state. The transient, nematic, disordered state induced by shear immediately after startup and unlocking translational degrees of freedom is thought to be an initial step that may be generic for other suspensions of strongly anisotropic colloids with important translation-orientation coupling induced by long-range interactions.

1 Introduction

With the fast progress of colloidal synthesis during the last decades, producing nanoparticles with well controlled shapes has been increasingly easy. Assembling or organizing these objects at the meso-scale opens routes for the design of new materials with interesting mechanical or optical properties such as, for example, photonic crystals with useful band gaps in the visible or highly transparent nano-composite barriers. [1–5]

Forming 3D colloidal crystals for such applications can already be quite challenging using spherical particles, but it is even more so for anisotropic colloids. Indeed, during relaxation in quiescent conditions, anisotropic shapes typically favor faster assembly processes by increasing the probability of short surface-to-surface distances compared to a system of spherical particles at the same volume fraction. This tends to promote increased local disorder and the stabilization of arrested states, such as glasses or gels. [6]

Applying an external field to a dynamically arrested system is not uncommon to overcome this difficulty. Classical examples are electric, magnetic, or hydrodynamic fields. In the present article, we present simulations showing how a shear-induced transition from a glassy state to a nematic crystal state can be triggered in a suspension of anisotropic nano-platelets reminiscent of Laponite clay. The expression "nematic crystal" is used here to refer to a 3D solid-like colloidal crystal with additional orientational order similar to that of a nematic phase.

Shear-induced ordering and shear induced crystallization have been observed since the 1970s for both colloidal hard spheres and soft charge-stabilized spheres both under steady and oscillatory shear. [7–12] Under steady shear, colloidal and non-colloidal suspensions of nearly hard spheres have been shown to exhibit shear-ordering above the freezing point, with strong concomitant changes in the self-diffusivity and relative viscosity. [13–16]. The ordered structures were often hexagonal lattices of strings aligned

[a] Laboratoire de Génie Chimique, Université de Toulouse, CNRS, INPT, UPS, Toulouse, France. E-mail: martine.meireles-masbernat@univ-tlse3.fr, yannick.hallez@univ-tlse3.fr
[b] FERMaT, Université de Toulouse, CNRS, INPT, INSA, UPS, Toulouse, France.
[c] Benjamin Levich Institute, City College of City University of New York, New York, USA. E-mail: morris@ccny.cuny.edu

† Electronic Supplementary Information (ESI) available: [details of any supplementary information available should be included here]. See DOI: 10.1039/cXsm00000x/

with the flow direction appearing for volume fractions ϕ larger than 0.5 and shear-melting at $\phi > 0.6$, but also layers aligned with the velocity-vorticity plane and sliding one over another, or bundles aligned with the flow direction.[17,18] Shear-ordering has been observed in Brownian suspensions only for Péclet numbers greater than one, which highlights the necessity for hydrodynamic forces to overcome thermal forces in order to impose a new structure. At very high shear rates, hydrodynamic interactions may however introduce chaos in the system again and ordered structures shear-melt into a liquid-like phase.[5,16]

Hard sphere suspensions actually order more easily under oscillatory shear than under steady shear. They can form different phases such as strings, stacked layers, face-centered cubic lattices or hexagonal close-packed lattices.[10,19–21] Crystallization occurs in oscillatory shear when the strain amplitude is above the yield strain.[20] Shear-induced structures are stable after flow cessation in suspensions initially in a glassy state, and not in suspensions initially in a liquid state.[10,17,19] Indeed, an initial arrested state ensures that colloidal interactions are strong enough to overcome the disordering introduced by thermal fluctuations in quiescent conditions.

Although suspensions of hard spheres have been more extensively studied, other types of soft or anisotropic particles can be ordered by applying a shear flow. Elastic particles,[22] microgels,[23] droplets,[24,25] star polymers,[26] or charge stabilized colloids[27–29] have been ordered using shear flows with the appearance of crystal, layered, or string phases. Once again, if initially jammed, these soft systems can form crystalline structures under steady and oscillatory shear that persist after flow cessation.[22,30]

Nano-particles with anisotropic shape or interactions are of special interest first because they are ubiquitous in nature, some members of this family being proteins, viruses, or mineral colloids, and second because their anisotropy can be used to tailor new useful mechanical or optical suspension properties. Anisotropic particles can arrange themselves at rest following many ordered structures including those mentioned above and many others inaccessible to uniform spheres, like nematic states, plastic crystals, columnar phases, or empty liquids, among other examples.[31–39] Anisotropic colloids generally exhibit a greater sensitivity to shear than spheres. For example, homonuclear dicolloids (dumbbells) can exhibit a transition from a layered structure without positional and orientational order at rest to what would be consistent with a plastic crystal at moderate shear rates.[40] Even a weak anisotropy has a significant impact on phase transitions.[39]

As we are most interested here by systems with shear-induced structures stable after flow cessation, focus will be put on initially arrested disordered anisotropic suspensions. Glassy states exist in two versions in suspensions of non-spherical particles due to the additional rotational degrees of freedom: plastic glasses have localized centers of mass and free rotations, and double glasses have both translational and orientational degrees of freedom frozen.[41,42] The yielding of such states when shear is applied is thus quite complex and depends on the particle geometry. For example, yielding is a two-step process for uniaxial particles with low aspect ratio, with rotations unlocked first and translations following. However, it is a one-step process for slightly more anisotropic particles due to the strong translation-rotation coupling.[42–44] The cage escape mechanism for uniaxial particles with larger, but still modest (in the range 2-4), aspect ratios has been shown to be associated more to center of mass motion than to rotation, qualitatively in line with Onsager's excluded volume mechanism for the nematic liquid crystal transition for long and thin particles.[42]

In this article, we report on a glass-to-nematic crystal transition observed in simulations of anisotropic platelet suspensions. Considering the important role of hydrodynamic interactions in the shear-ordering process, and in order to measure the mechanical response of the suspension during transitions, we use an extension of Accelerated Stokesian Dynamics (ASD) to resolve many-body hydrodynamic interactions in a suspension of anisotropic colloids. The no less important electrostatic interactions between colloidal platelets are accounted for using a site model with charge renormalization.

As an example of platelet suspension, we choose a model system resembling the Laponite clay as closely as possible. Clays are widely used in the industry as texturing agents, in particular because of their capacity to confer a pasty consistence to a complex fluid at very low volume fraction. For this reason, the clay family has been studied experimentally extensively, and in particular the Laponite type which is a synthetic clay quite simpler than natural ones in many regards. It is rather monodisperse, with a smaller aspect ratio, and with a well documented chemistry. Although many Monte Carlo and Brownian dynamics simulations have been undertaken so far, mainly in quiescent conditions, we believe this work to be a first attempt at including both many-body hydrodynamics and surface charge renormalization in simulations of sheared clay-like suspensions.

In this paper, the numerical method is first presented. The structure of a suspension of clay-like platelets in quiescent conditions is then reported as a function of volume fraction and electrostatic interaction range. The shear-ordering of an initially glassy sample is then demonstrated and the mechanisms at play during the phase transition are discussed. In particular, it will be shown that a transition from a glassy state to a nematic crystalline order can be obtained in a two-step process with shear providing incomplete ordering at first, and with subsequent relaxation in quiescent conditions to reach the crystal in a second stage.

2 Simulation method

Simulating rigorously a flowing suspension of anisotropic charged colloids at finite density is a formidable task owing to the geometrical complexity and to the many-body nature of hydrodynamic and electrostatic interactions. More tractable simulations can be envisaged if some aspects of the problem can be coarse-grained while keeping the essential physics. The next two sections detail the numerical strategies used to compute many-body hydrodynamic interactions and to coarse-grain electrostatic interactions while still accounting for charge renormalization and respecting the reduced temperature of a realistic Laponite system.

2.1 Hydrodynamics

The simulation technique used in this work is based on the Accelerated Stokesian Dynamics (ASD) method for Brownian suspensions of spheres. In brief, because the Reynolds and Stokes numbers are small in a colloidal suspension, the translational/rotational velocity of each sphere $\boldsymbol{U_s}$ is related to the Brownian and colloidal interaction forces (also including the torques, in a compact notation) $\boldsymbol{F_s^b}$ and $\boldsymbol{F_s^p}$ and to the stresslets $\boldsymbol{S_s}$ they experience by the overdamped Langevin equation

$$-\boldsymbol{\mathscr{R}}\cdot\begin{bmatrix}\boldsymbol{U_s}-\boldsymbol{u_s^\infty}\\ -\boldsymbol{E^\infty}\end{bmatrix}+\begin{bmatrix}\boldsymbol{F_s^b}+\boldsymbol{F_s^p}\\ -\boldsymbol{X_s}\boldsymbol{F_s^p}\end{bmatrix}=\begin{bmatrix}\boldsymbol{0}\\ \boldsymbol{S_s}\end{bmatrix}, \tag{1}$$

where $\boldsymbol{X_s}$ is the generalized configuration vector of the spheres, $\boldsymbol{u_s^\infty}$ is the velocity of the imposed background shear flow at the center of each sphere, $\boldsymbol{E^\infty}$ is its associated rate of strain, and

$$\boldsymbol{\mathscr{R}}=\begin{bmatrix}\boldsymbol{R_{FU}} & \boldsymbol{R_{FE}}\\ \boldsymbol{R_{SU}} & \boldsymbol{R_{SE}}\end{bmatrix} \tag{2}$$

is a grand resistance matrix giving the hydrodynamic forces, torques ("F" subscript representing the combined force/torque) and stresslets ("S" subscripts) exerted on the spheres as a function of the background flow and of the flow perturbations associated to motion of the spheres ("U" and "E" subscripts). In essence, the core of the ASD method is to solve (1) self-consistently and without inverting the large resistance matrix so the solution $\boldsymbol{U_s}$ and the configurations obtained by solving $d\boldsymbol{X_s}/dt=\dot{\boldsymbol{X}}_s=\boldsymbol{U_s}$ are such that the fluctuation-dissipation theorem is respected. ASD can be considered as an extension of Brownian dynamics in which many-body hydrodynamic interactions are accounted for consistently. More details are given in the original articles.[45,46]

This method cannot be used directly to simulate suspensions of plate-like colloids because the resistance functions for interactions of particles are available only for spheres and certain ellipsoids.[47] In this work, anisotropic colloids are thus coarse-grained as non-deformable clusters of spheres (see Fig. 1). The motion of each individual sphere is obtained by solving (1) combined with rigid body constraints for the spheres belonging to the same cluster.[48–50] Denoting $\boldsymbol{U_c}$ the translational/rotational velocities of clusters with configuration $\boldsymbol{X_c}$ and $\boldsymbol{u_c^\infty}$ the translational/rotational background flow velocity at the center of the cluster, the constraints can be written

$$\boldsymbol{U_s}-\boldsymbol{u_s^\infty}=\boldsymbol{\Sigma}^T\cdot(\boldsymbol{U_c}-\boldsymbol{u_c^\infty})-\begin{bmatrix}\boldsymbol{E^\infty}\cdot(\boldsymbol{X_s}-\boldsymbol{X_c})\\ \boldsymbol{0}\end{bmatrix}, \tag{3}$$

where $\boldsymbol{\Sigma}^T$ is obtained by assembling the smaller tensors relating the velocity of each sphere s to that of the cluster it belongs to c

$$\boldsymbol{\Sigma}^T_{s\in c}=\begin{bmatrix}1&0&0&0&(\boldsymbol{X_s}-\boldsymbol{X_c})_3&-(\boldsymbol{X_s}-\boldsymbol{X_c})_2\\ 0&1&0&-(\boldsymbol{X_s}-\boldsymbol{X_c})_3&0&(\boldsymbol{X_s}-\boldsymbol{X_c})_1\\ 0&0&1&(\boldsymbol{X_s}-\boldsymbol{X_c})_2&-(\boldsymbol{X_s}-\boldsymbol{X_c})_1&0\\ 0&0&0&1&0&0\\ 0&0&0&0&1&0\\ 0&0&0&0&0&1\end{bmatrix}. \tag{4}$$

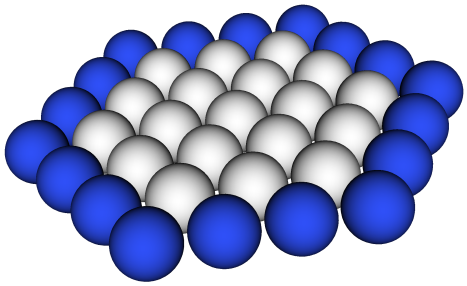

Fig. 1 Coarse-grained anisotropic plate-like colloid with aspect ratio 7.3 (AR7). The thickness is $h=2a$ with a the radius of the spheres and the diameter $D=2R$ corresponds to 7 spheres plus 6 small gaps of $0.05a$ between them. Blue and white spheres carry partial effective charges $Z_{\text{rim}}e$ and $Z_{\text{face}}e$, respectively.

The forces/torques exerted on clusters are related to the forces/torques exerted on the spheres by

$$\boldsymbol{F_c}=\boldsymbol{\Sigma}\cdot\boldsymbol{F_s}. \tag{5}$$

Using (3) in (1) and multiplying the first line of this equation by $\boldsymbol{\Sigma}$ yields the evolution equation relating the cluster translational/angular velocity $\boldsymbol{U_c}$ to the forces exerted on each sphere in the suspension

$$\begin{aligned}-\boldsymbol{R_{FU}^c}\cdot(\boldsymbol{U_c}-\boldsymbol{u_c^\infty})+\boldsymbol{\Sigma}\cdot\boldsymbol{R_{FU}}\cdot\boldsymbol{E^\infty}\cdot(\boldsymbol{X_s}-\boldsymbol{X_c})\\ +\boldsymbol{\Sigma}\cdot\boldsymbol{R_{FE}}:\boldsymbol{E^\infty}+\boldsymbol{\Sigma}\cdot(\boldsymbol{F_s^b}+\boldsymbol{F_s^p})=\boldsymbol{0},\end{aligned} \tag{6}$$

where $\boldsymbol{R_{FU}^c}=\boldsymbol{\Sigma}\cdot\boldsymbol{R_{FU}}\cdot\boldsymbol{\Sigma}^T$ appears as a resistance tensor associated to the hydrodynamic interactions between clusters. This equation is solved in a manner similar to that used for ASD for spheres after $\boldsymbol{R_{FU}^c}$ has been computed. Additional details can be found in Refs. 48–51.

Note that it is also possible to force an almost rigid body motion by linking spheres belonging to the same platelet with springs. This choice was used by Kawabata et al. to simulate the structure of a plate-like particle suspension under shear by solving the Navier-Stokes equation directly and coupling it to a discrete element method for the particles.[52]

2.2 Electrostatics

The structure and dynamics of colloidal suspensions strongly depend on electrostatic interactions. Here, the effect of anisotropic interactions is introduced by ascribing different partial charges to the individual spheres making up the plate-like particles.

For the model plate-like particles with aspect ratio 7.3 (AR7) used in this work, 18 spheres are located on the "rim" and carry Z_{rim} positive charges each, and 19 spheres are considered to constitute the "faces" and carry Z_{face} negative charges each. Electrostatic interactions between two platelets i and j are then modelled using a sum of hard-sphere Yukawa potentials

$$\boldsymbol{F_{c,ij}}=\sum_{k\in i}\sum_{l\in j}Z_kZ_l l_B kT\left[\frac{e^a}{1+\kappa a}\right]^2 e^{-\kappa r_{kl}}\frac{1+\kappa r_{kl}}{r_{kl}^2}\hat{\boldsymbol{r}}, \tag{7}$$

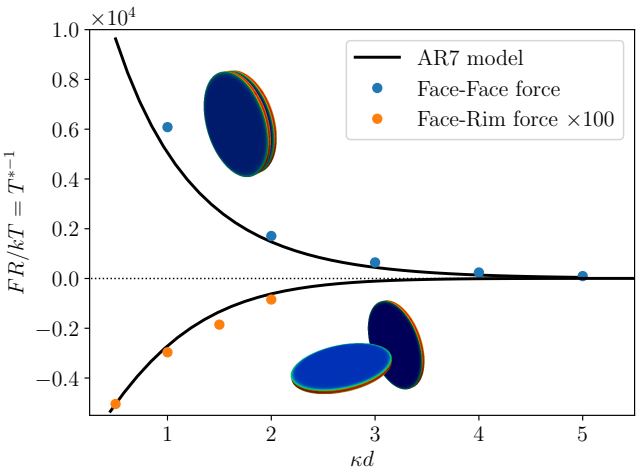

Fig. 2 Symbols: "exact" interaction forces computed by solving the 3D Poisson-Boltzmann equation for Laponite platelets for $\kappa^{-1} = 1$ nm. Lines: force model (7) obtained by optimization of Z_{rim} and Z_{face}. d is the distance of closest approach between platelets. Colors on the platelet images are color maps of the electrostatic potential field.

where Z_k and Z_l are either Z_{face} or Z_{rim} depending on the positions of spheres k and l, $l_B = e^2/4\pi\varepsilon kT$ is the Bjerrum length, e is the unit charge, kT is the thermal energy, κ^{-1} is a screening length, r_{kl} is the distance between the centers of spheres k and l belonging to platelets i and j respectively, and $\hat{\boldsymbol{r}}$ is the unit vector along this line.

The Yukawa form and the additivity approximation are, in principle, valid only for weak charges and large separation distances. However, this has been shown to be a reliable form for more concentrated suspensions and strongly charged particles provided the charges and the screening length are suitably redefined. This procedure known as *charge renormalization* can be performed using different strategies.[53–58] Here, the effective partial charges Z_{face} and Z_{rim} to be used in model (7) are fixed so the resulting scaled force magnitude $F_c R/kT$ is equal to the one that would be applied on Laponite platelets at the same separation distance. This constraint ensures that the force balance between electrostatic and thermal effects is the same in the model AR7 suspension and in a Laponite suspension. Formulated differently, the reduced temperature $T^* = kT/F_c R$ is the same in both suspensions. More precisely, T^* is matched between Laponite and AR7 models in face-face and face-rim interaction configurations simultaneously. The former is important for glassy suspensions dominated by the strong net charge provided by faces and the latter is the major attractive interaction configuration typical of the House of Cards (HoC, see Fig. 4) structure often reported for clay gels.

Reference interaction force profiles have first been computed using the Laponite geometry and surface charge distribution. Two flat, cylindrical particles with radius $R = 15$ nm and thickness $h = 1$ nm were fixed in a large domain in face-face or face-rim configuration (see Fig. 2). They carried 70 positive charges along the rim and 350 negative charges on each face. These charges were smoothed as uniform surface charge densities σ on the corresponding faces. The non-linear Poisson-Boltzmann (PB) and Laplace equations (using $\Delta = \nabla \cdot \nabla$)

$$\begin{cases} \Delta\psi &= \kappa_r^2 \sinh\psi \\ \Delta\psi^s &= 0 \end{cases} \tag{8}$$

were solved in the fluid and solid phases, respectively, to obtain the electrostatic potential fields ψ and ψ^s scaled by kT/e. In (8), $\kappa_r = \sqrt{8\pi l_B n_r}$ is an inverse screening length involving the salt density n_r at a point where $\psi = 0$. The coupling between these equations is enforced on the surface of the particles through the Gauss condition

$$(\varepsilon \boldsymbol{E} - \varepsilon^s \boldsymbol{E}^{\boldsymbol{s}}) \cdot \boldsymbol{n} = \sigma \tag{9}$$

where $\boldsymbol{E}^{(\boldsymbol{s})}$ is the electric field computed from $\psi^{(s)}$ and $\boldsymbol{n}$ is the unit vector normal to the surface of the colloids. The excess osmotic stress tensor

$$\boldsymbol{\tau} = -2n_r kT(\cosh\psi - 1)\boldsymbol{I} + \varepsilon\left[\boldsymbol{E}\otimes\boldsymbol{E} - \frac{1}{2}\boldsymbol{E}^2\boldsymbol{I}\right], \tag{10}$$

is then used to obtain the force exerted on colloids of surface S

$$\boldsymbol{F_c} = \int_S \boldsymbol{\tau}\cdot\boldsymbol{n} dS. \tag{11}$$

The numerical solution of the boundary value problem (8)-(9) and the integration (11) were performed with a level-set method described in Refs. 59–61. These calculations can be undertaken at high surface charge density because the non-linear PB equation is solved. The limitations are those of the PB theory: results are valid only in the weak electrostatic coupling limit and when the finite size of ions is unimportant. In practice (but this is not a rigorous rule) these conditions are often met in suspensions with monovalent ions at concentrations lower than 0.1 M.

The face-face and face-rim scaled force profiles obtained from these simulations are then fitted simultaneously with model (7) by adjusting the effective partial charges (see Fig. 2). Values $Z_{\text{face}} = -15.39$ and $Z_{\text{rim}} = 5.96$ were found for $\kappa^{-1} = 1$ nm. The total net charge is thus $-185e$. In principle, effective charges depend on the screening length but they were kept constant throughout this work for simplicity.

3 Quiescent Structure

In the weak electrostatic coupling limit, the quiescent structure of anisotropic platelet suspensions is determined by four dimensionless parameters, namely the volume fraction ϕ, the aspect ratio (AR) of platelets D/h, the inverse electrostatic interaction range κD, and the reduced temperature T^*. As detailed in the previous section, the aspect ratio and T^* have been fixed with the aim of obtaining a coarse-grained model of platelets as close as possible to Laponite. Hence the phase diagram of AR7 suspensions ($D/h \simeq 7$) is presented in the $(\phi, \kappa D)$ plane in Fig. 3a.* The different structures that have been observed under quiescent conditions are detailed shortly hereafter.

For interaction ranges large compared to the mean inter-

* Note that the volume fraction of a suspension of coarse grained platelets is defined throughout this paper as the volume of the spheres constituting the platelets divided by the total volume of the simulation box.

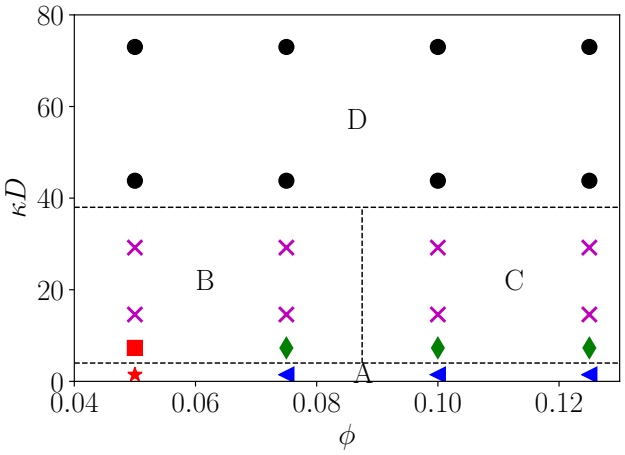

(a) **A** Repulsive glass, **B** Phase separation, **C** Equilibrium gel, **D** Liquid-like structure. Red star: non-connected glass (Fig. 3c); blue triangles: bonded glass with particles in contact with OC configurations; red square: structure with particles mainly in OC configuration (Fig. 3d); green diamonds: particles in both OC and HoC configurations; purple crosses: HoC configurations (Fig. 3e 3f); black circles: liquid-like phase (Fig. 3g).

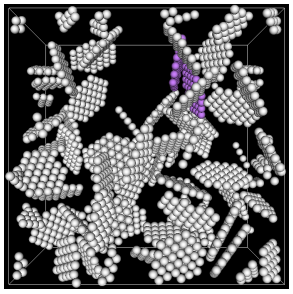

(b) Initial spatial configuration.

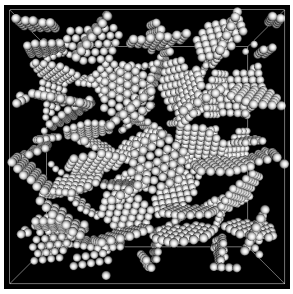

(c) $\kappa D = 1.46$. Wigner glass (red star in Fig. 3a, region A).

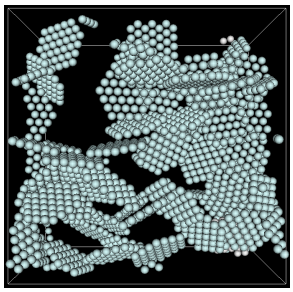

(d) $\kappa D = 7.3$. Mainly OC (red square in Fig. 3a, region B).

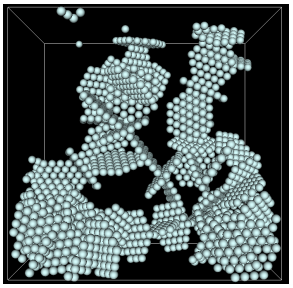

(e) $\kappa D = 14.6$. Mainly HoC (purple cross in Fig. 3a, region B).

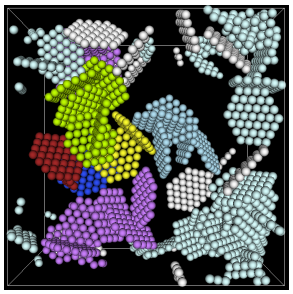

(f) $\kappa D = 29.2$. Mainly HoC (purple cross in Fig. 3a, region B).

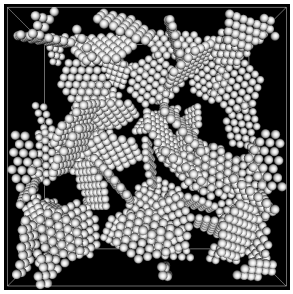

(g) $\kappa D = 73$. Liquid-like structure (black circle in Fig. 3a, region D).

Fig. 3 "Phase diagram" of a suspension of AR7 particles (a) and structures at $\phi = 0.05$ and different interaction ranges (b)-(g). Non-bonded platelets appear in white and platelets sharing some bonds are represented with a unique non-white color.

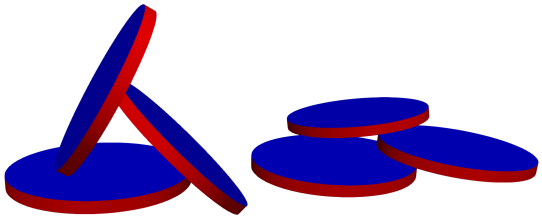

Fig. 4 Sketches of the house-of-card (HoC, left) and overlapping coin (OC, right) local configurations.

particle distance, *i.e.* in the electrostatically concentrated regime, the incoherent intermediate scattering function remains very high at all times ($F > 0.96$), indicating strongly arrested states and the short-time diffusion coefficients D_s remain quite high and independent of aging time t_w (see Fig. 3 and 4 in SI). This signature is very reminiscent of the "rattling in the cage", and therefore systems in region A in Fig. 3a are classified as glassy. Examining the details of the microstructure reveals the existence of two types of glasses. At low volume fraction, the structure is a classical Wigner glass with no inter-particle contact. Particles are trapped in electrostatic cages by the repulsive long-range interactions due to their large negative net charge (Fig. 3c). At sufficient volume fractions, the suspension is still globally repulsive (see osmotic pressure and structure factors in Fig. 5 and 6 in SI) but some platelets are close enough for face-rim attractions to rotate them and generate some bonds. Examining radial and angular distribution functions (Fig. 9 and 10 in SI) reveals that these bonds are mainly of the overlapping coin type (OC, see Fig. 4 for a sketch). In these physico-chemical conditions, the edge-face attractions are thus likely to reduce the overall osmotic pressure significantly compared to a system with the same geometry but without charge anisotropy. These two types of glasses are very reminiscent of the non-bonded and bonded glasses identified by Zaccarelli and Poon for dense suspensions of spheres with short-range attractions.[62] For the present anisotropic platelets, the short-range character of attractions is due to the large charge anisotropy that makes interactions repulsive if platelets are too far away. Note that the large ranges of interactions necessary to obtain glasses in the present simulations cannot be reached in aqueous Laponite suspensions, even after deionization, due to the presence of a significant concentration of free counterions. Other solvents like DMSO can be used to obtain large enough interaction ranges.

In the electrostatically dilute case ($\kappa D > 40$ here), short range interactions are unable to hinder the thermal motion of platelets significantly and a fluid-like phase is observed as expected (see radial and angular distribution function in Fig. 19 in SI). Platelets are rather randomly oriented and they do not bond within the simulation time as revealed by their white color in Fig. 3g. Note that van der Waals forces not included here will often have an important role for these high-salt conditions and that aggregation is likely to occur in practice.[63]

The influence of the charge anisotropy of the platelets is most important at intermediate interaction ranges. For $5 < \kappa D < 40$, an aggregated structure is always obtained (see the light-blue network in Fig. 3d– 3f). The short-time diffusion coefficients are

decreasing with aging time (Fig. 13 in SI), indicating a progressive strengthening of bonds. The osmotic pressure is either very low at $\kappa D = 7.3$ or oscillating around zero for larger interaction ranges as a result of the combined action of electrostatic attractions and hard core exclusion (Fig. 5 in SI). These systems are therefore attractive and aging. There is no global orientational order, as indicated by the nematic order parameter that is below 0.25. In the dilute region B, the structure factor keeps increasing with time at small wavevector q (corresponding to large-scale structure) whereas it saturates in the more concentrated region C (see Fig. 12 in SI). Region B therefore corresponds to phase separation, while region C is a percolated gel phase without large scale density fluctuations at least on the time scale of the simulations. The same behavior was observed by Ruzicka et al. in Laponite suspensions.[64] The transition is found here at $\phi \simeq 0.08$ whereas for Laponite is was found around $\phi \simeq 0.004$. The comparison may be clearer using an effective volume fraction ϕ^{eff} in which the effective volume of each platelet is assumed to be a sphere of radius $R + \kappa^{-1}$. In the experiments, the B-C transition is around $\phi^{\text{eff}} \simeq 2.2$ and in the present simulations it is somewhere between 0.5 and 2. In both cases this transition appears when ϕ^{eff} is close to 1, which is the critical volume fraction above which double layers overlap in the randomized structure at initial time so aggregation can take place almost instantaneously, without significant particle diffusion. In this case, structural arrest occurs rapidly, such that the structure factor appears to be independent of time. On the other hand, at $\phi^{\text{eff}} < 1$ particles have time to diffuse before attractive electrostatic interactions trigger aggregation. This takes place on considerably longer time scales and leads to the growth of (eventually percolated) aggregates, with an associated increase of the structure factor at low q with time. Within the percolated regions B and C, the most frequent platelet arrangement is found to be the HoC configuration that has been classically reported for clays. Near the limit with glasses ($\kappa D \simeq 4.5$), some OC (overlapping coin) configurations are mixed with HoC at high volume fraction, and these can even be the only type of contact at low volume fraction (Fig. 3d). These microstructural details can be verified with the radial and angular correlation functions and with the bond angle distribution reported in Fig. 14, 15, 17 and 18 in SI). The main parameters used to understand the nature and the microstructure of phases A, B, C, and D are summarized in Table 1.

The structures obtained without shear flow are in good agreement with those found in previous experimental and numerical studies. Ruzicka and coworkers considered plate-like colloids with a purely attractive force model.[64] They also detected two types of attractive systems with either phase separation at low density or equilibrium gel (or empty liquid) at high density. In their MC simulations of anisotropically charged platelets, Delhorme et al. reported attractive systems ("cluster fluid" and gel) at intermediate interaction range with a transition from OC dominated contacts to HoC dominated contacts when increasing the volume fraction.[65] They did not observe a glass as they did not consider very long range interactions. One phase observed by these authors and absent here is the liquid crystalline smectic B phase. In their work, it is obtained at high charge anisotropy and in a limited region of interaction range and volume fraction. Further comments on this phase will be proposed hereafter. Ordered suspensions of plate-like particles such as columnar phases, or BCC or hexagonal crystals, have been reported at volume fractions higher than those investigated here by Delhorme et al.[66] with anisotropically charged clay-like platelets, and in purely repulsive nanodisk suspensions by Jabbari et al.[35,36]. Crystalline order has not been observed at the moderate volume fractions considered here in quiescent conditions, but a glass-to-crystal transition can be triggered by application of shear as shown in the next section.

4 Shear-induced ordering

The strength of a shear flow is characterized by the shear rate $\dot{\gamma}$, with the associated time scale $\dot{\gamma}^{-1}$. Brownian motion is characterized by a pair relative diffusion coefficient $2D_0$ where $D_0 = kT/6\pi\eta_0 a$ is the single particle self-diffusion coefficient at infinite dilution. A time scale associated to Brownian motion can thus be defined as $\tau_B = a^2/2D_0$. The ratio of this Brownian time scale and the shear time scale defines the Péclet number $Pe = 3\pi\eta_0 a^3\dot{\gamma}/kT$. Denoting as F^E the order of magnitude of electrostatic forces, a time scale for migration due to these forces is $\tau_E = \eta_0 R^2/F^E$. We thus also introduce a Mason number $Ma = \eta_0 R^2\dot{\gamma}/F^E$ as the ratio of the electrostatic migration time scale and the shear time scale. In what follows $Ma = 1$ and $Pe \gg 1$ when shear is applied, unless specified otherwise.

Shear has been applied to all the structures presented in the previous section. It has been applied in particular to the gel state most often observed in rheology experiments involving clay suspensions. When subject to a shear flow, these percolated structures are increasingly broken and eroded as the shear rate increases. The classical shear-thinning and thixotropic behavior well known for clay suspensions has been observed in the present simulations but it will be the subject of another article. Here we rather focus on the observation of shear-ordering for initially glassy suspensions. Therefore, in the next two sections, we report the structure evolution during shear and after flow cessation for an AR7 platelet suspension at $\phi = 0.05$ and $\kappa D = 1.46$.

4.1 Shear period

Shear-induced ordering has been evidenced using the following simulation protocol. A first reference simulation without shear is performed for more than 80 units of Brownian time τ_B, until an arrested state is reached (green curve in Fig. 5 and Fig4Green movie in SI). In the second simulation, a first relaxation period in quiescent conditions is imposed for $25\tau_B$ in order to obtain the glassy state. At this point, this simulation is identical to the first one. Then shear is applied for 30 units of time $\dot{\gamma}^{-1}$ (blue curve in Fig. 5), and after the shear period the suspension is left to relax again in quiescent conditions for 30 additional units of time τ_B, until a new arrested state is reached. The last relaxation period will be referred to as the recovery period. A movie (Fig4Blue) of this relaxation/shear/recovery sequence corresponding to the blue curve in Fig. 5 is provided in SI.

Throughout this article, shear is applied at $Pe \gg 1$ so the flow-

observable	region A	region B	region C	region D
$D_s(t_w)$	constant and high	$\searrow$ with t_w	$\searrow$ with t_w	not measured
Osmotic pressure	high, $\nearrow$ with ϕ	$\simeq 0$	$\simeq 0$	$\simeq 0$
$S(q \to 0)$	stable	$\nearrow$ with t_w	stable	stable
bonds	no bonds or a few clusters	percolation	percolation	no bonds
structure	homogeneous	heterogeneous	homogeneous	homogeneous and $g(r) \simeq 1$

Table 1 Main structural and dynamical parameters used to characterize phases A, B C, and D in Fig. 3a. $D_s(t_w)$ denotes the aging time dependence of the short-time diffusion coefficient. $S(q \to 0)$ represents the low wavenumber limit of the structure factor.

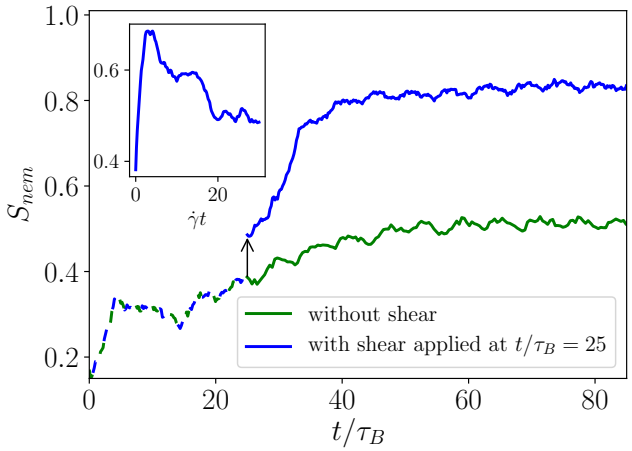

Fig. 5 Main figure: evolution of the nematic order parameter S_{nem} in quiescent conditions following shear-induced ordering (blue line) or without shear-induced ordering (green dashed line). Inset: evolution of S_{nem} during shear. Shear is applied at $Pe \gg 1$ so the duration of the shear period is virtually zero on the scale of the main figure.

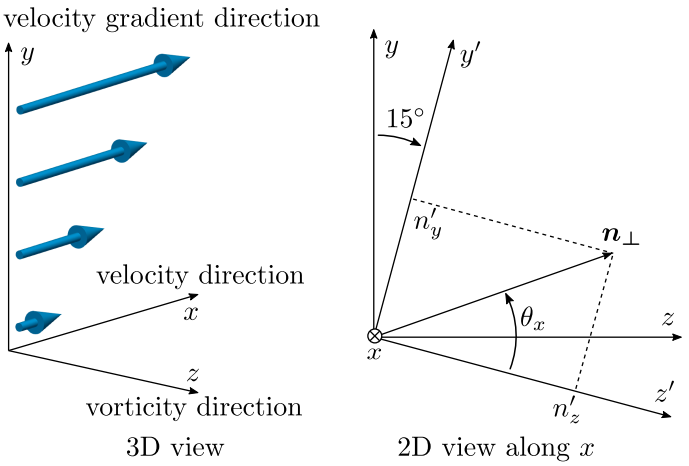

Fig. 6 Sketch introducing the (x,y,z) frame, the (x,y',z') frame, and the angle θ_x given the projection $\boldsymbol{n}_\perp$ of a vector $\boldsymbol{n}$ on the (x,y) plane. Indices 1, 2, and 3 will be used for directions x, y, and z, respectively.

ing state is governed solely by hydrodynamic and electrostatic effects and can be described in terms of Ma only, neglecting Brownian motion. Shear-induced ordering has been observed for simulations at $Ma = 1/4$, 1, and 4, and not in simulations at $Ma = 100$ or $Ma \to \infty$ (zero charge).

The nematic order parameter S_{nem} provided as a function of time in Fig. 5 is already a good evidence of shear-induced ordering. It is the largest eigenvalue of the ordering tensor

$$Q_{ij} = \frac{1}{2}\langle 3 n_i n_j - \delta_{ij} \rangle, \tag{12}$$

where brackets denote a particle average and $\boldsymbol{n}$ is the unit vector normal to each platelet. S_{nem} is comprised between 0 for random orientations and 1 for perfectly aligned platelets. In the glassy state considered here, S_{nem} is never larger than about 0.5 without shear. Immediately after the application of shear, it increases sharply as the flow tilts every platelet and then it relaxes progressively to a value of 0.5, similar to the non-sheared suspension. At this point, it seems shear did not help to structure the suspension. However, S_{nem} increases again just after flow cessation to reach a value larger than 0.8 indicating the appearance of significant nematic order. The mechanisms behind this intriguing transition are detailed hereafter, in particular how the shear-induced incomplete correlations can unlock crystallization in the recovery period.

The lack of any positional ordering before shear is applied can be verified in Fig. 7a and 8a, while a very distinctive positional order is observed at the end of the period of shear (see Figs. 7b and 8b). From a quick look at the snapshots in Fig. 7b, the most striking feature is the appearance of a tilted hexagonal pattern in the gradient-vorticity plane. The tilt angle appears in order to accommodate the imposed periodic boundary conditions. To analyse this structure, a frame (x,y',z') based on the symmetry axes of the hexagonal pattern is introduced. It is obtained with a 15° rotation of the (x,y,z) frame around the x axis (see Fig. 7b).

A statistical characterization of the structure under steady shear is presented in Fig. 8b. The hexagonal structure in the gradient-vorticity plane is indeed confirmed with very clear Bragg-like spots at distances $2.2R$ and $2.2R\sqrt{3}$ (see Fig. 8b-center). Because strings at different y positions advance at different velocities in the shear flow, there are no positional correlations in the x direction across different strings as indicated by the white strips at $z' = 2.2R$ in Fig. 8b-right and at $y' = 2.2R\sqrt{3}$ in Fig. 8b-left. Positional correlations do exist within one string though, as revealed by the spots at $y = y' = 0$ in 8b-left. The two x-separations with highest probability correspond to spots 2 and 5 and are associated to distances $2R$ and $4R$ in the flow direction. They correspond to just-touching platelets, e.g. those in green in Fig. 7b. For these specific locations, colloids are oriented according to two almost equally preferred relative angles of about 5° and 60° (Fig. 9a). Two touching platelets slightly favor the 60° configuration (spot 2) and two platelets in the same

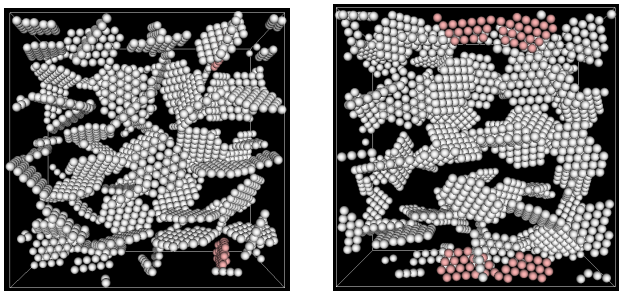

(a) Structure after relaxation in quiescent conditions only (green curve in 5 at $t > 80$).

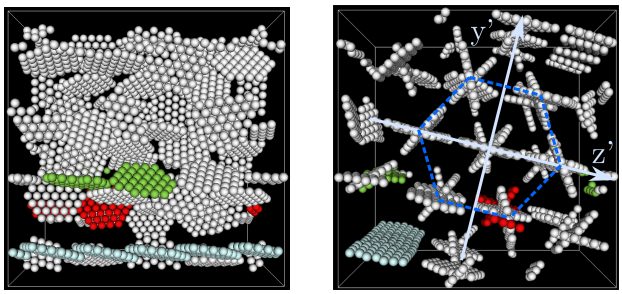

(b) Structure at the end of the period of shear (inset of Fig. 5 at $\dot{\gamma}t > 20$).

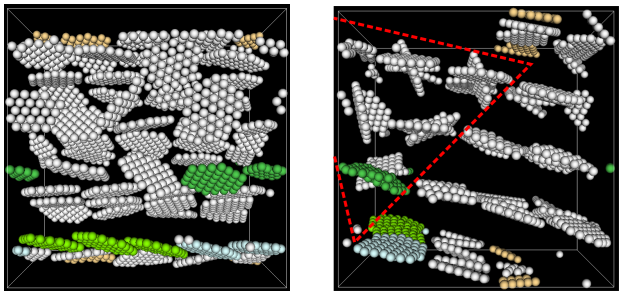

(c) Structure after relaxation in quiescent conditions following a period of shear (blue curve in 5 at $t > 80$).

Fig. 7 Microstructure seen in the $x-y$ (velocity-gradient, left) and $y-z$ (gradient-vorticity, right) planes. The tilted (x, y', z') frame is indicated in 7b and 7c. Non-bonded platelets appear in white and platelets sharing some bonds are represented with a unique non-white color.

string but separated by a third platelet slightly favor the 5° configuration (spot 5). The other most probable distances along the x direction are given by spots 1 and 4 in Fig. 8b-left., with corresponding distances $1.6R$ and $3.2R$. For these platelets, the relative angle distribution function is sharply peaked about 0° (Fig. 9a). This corresponds to parallel platelets locked in OC configuration in strings, for instance the light blue one visible at the bottom of Fig. 7b. Spot 3 involves a distance of $2.6R$ and no particular angular correlation (data not reported). It is believed to be associated with defects. So to summarize, within one string two consecutive platelets are most of the time just touching and have a relative angle of 60 degrees. A less frequent configuration also exists, namely a string of parallel platelets in overlapping coin configuration. These two types of configurations can be easily observed in the Fig4Blue movie provided in SI.

Although positional correlations in the x direction are not observed *between different strings*, some strong orientational correlations are found: platelets arrange either at 10° or at 60° with equal probability as shown in Fig. 9b. At first, the 60° angle might be thought to be an effect of electrostatic rim-face attractions similar to what leads to the HoC configuration, but the fact that this angle disappears immediately after flow cessation clearly indicates that it is induced at least partly by hydrodynamic interactions. The 10° preferred relative angle can be the signature of either (i) correlations between the OC strings mentioned above and other disconnected strings or (ii) a sort of slightly degenerate 0° configuration. Indeed, long range face-face electrostatic repulsions actually favor a nematic state as will be shown hereafter, but a perfect 0° angle between two neighbouring platelets could be prevented by local, less intense, rim-rim repulsions in this dense system.

Besides the two-platelet orientational correlations commented above, the one-platelet orientation probability is also of interest. One effect of the shear flow is to bring almost every platelet normal vector near the gradient-vorticity plane. Therefore, platelet orientations can be described quite well with the angle $\theta_x = \text{atan2}(n_{y'}/n_{z'})$ between 0° and 180°, the nematic state corresponding to $\theta_x = \pi/2$. Due to the symmetries of the system, considering the $[0, \pi/2]$ range is enough. The probability $P(\theta_x)$ of observing a platelet with orientation θ_x is reported in Fig. 10. At the end of the first relaxation period in quiescent conditions ($S_{nem} \simeq 0.4$ at $t = 25\tau_B$ in Fig. 5), a broad distribution of angles is observed with most platelets between 60° and 90°. At the end of the period of shear described above ($S_{nem} \simeq 0.5$ at $\dot{\gamma}t = 30$ in the inset of Fig. 5), the angle distribution shows a sharp peak between 80° and 90° and a wider peak around 30°. This is consistent with the 60° relative angle between two platelets mentioned above. This figure reveals that although the global nematic order is not really high under shear, the suspension is actually very orientationnally ordered.

Ordering induced by shear has been demonstrated above, but at this point the ordered structure is not perfect. Positional correlations in the gradient-vorticity plane and along each string are obtained, but there are no positional correlations across different strings and the structure is not nematic. Quite strikingly, the next section will reveal that this puzzling structure evolves towards a

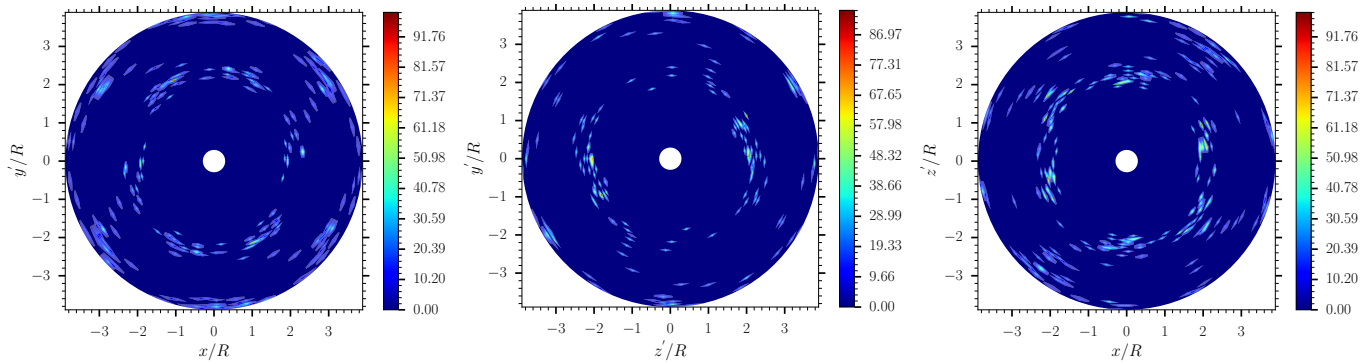

(a) Structure after relaxation in quiescent conditions only (green curve in 5 at $t > 80$).

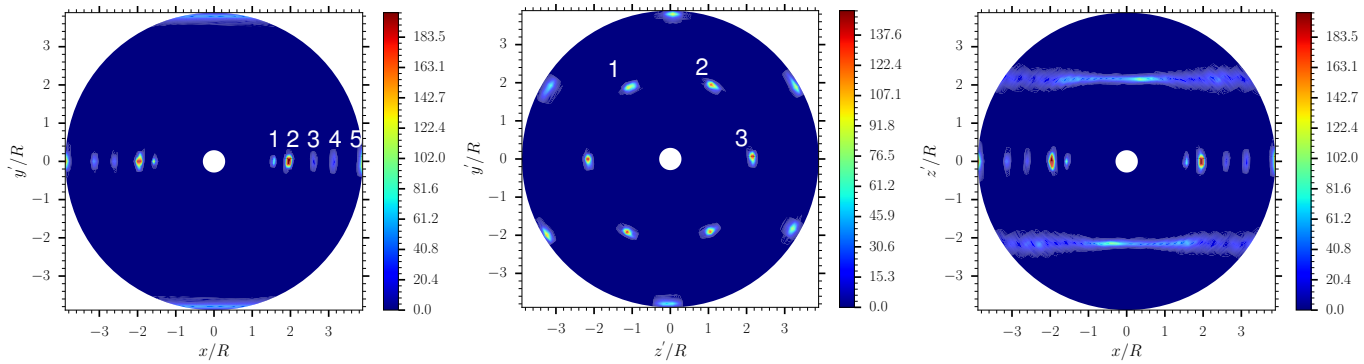

(b) Structure at the end of the period of shear (inset of Fig. 5 at $\dot{\gamma}t > 20$).

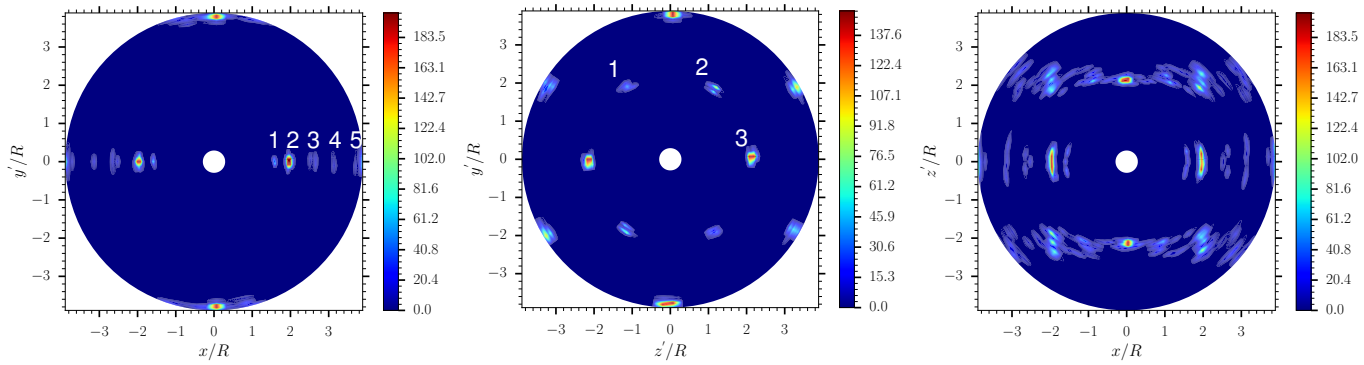

(c) Structure after relaxation in quiescent conditions following a period of shear (blue curve in 5 at $t > 80$).

Fig. 8 Radial distribution function $x-y'$ (left), $y'-z'$ (center), and $x-z'$ (right) planes. The (x,y',z') frame is defined as explained in the text. The $y'-z'$ plane is the gradient-vorticity plane.

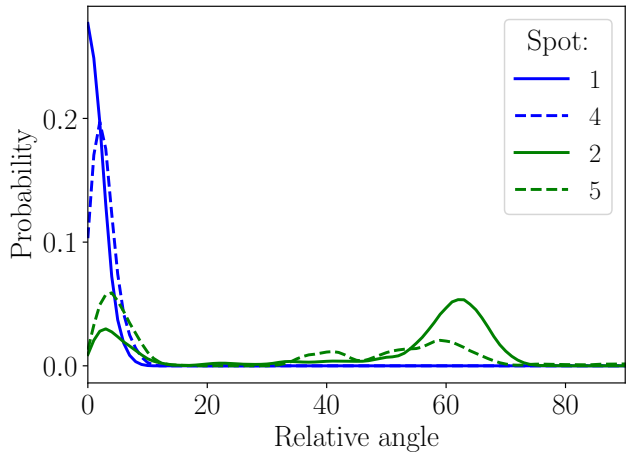

(a) Along one string. Spot numbers are identified in Fig. 8b-left.

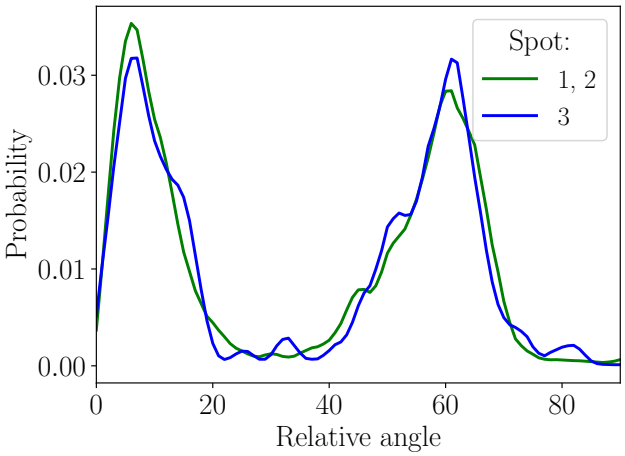

(b) Across different strings. Spot numbers are identified in Fig. 8b-center.

Fig. 9 Probability of relative angles between platelets at the end of the period of shear ($\dot{\gamma}t = 30$ in the inset of Fig.5). The relative angle between two platelets with unit normal vectors $\boldsymbol{n}$ and $\boldsymbol{m}$ is $\arccos(\boldsymbol{n}\cdot\boldsymbol{m})$.

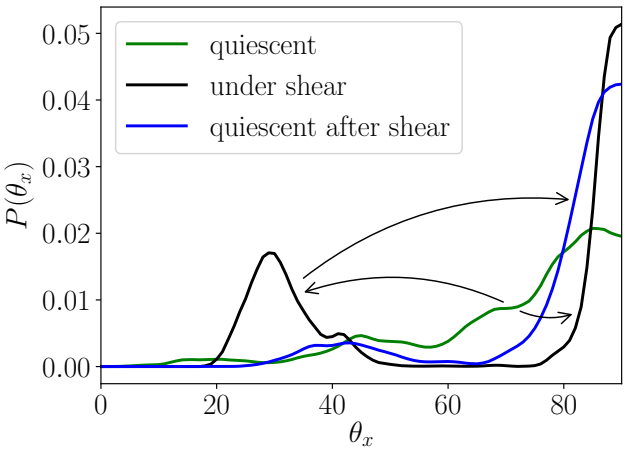

Fig. 10 Probability of orientation angle θ_x at the end of the first relaxation period in quiescent conditions ($t/\tau_B = 25$ in Fig. 5), at the end of the period of shear ($\dot{\gamma}t = 30$ in the inset of Fig. 5), and after full relaxation after flow cessation ($t/\tau_B = 80$ in Fig. 5). Arrows describe the chronology of the distribution evolution.

nematic hexagonal crystal after flow cessation.

4.2 Relaxation after shear

The structure obtained after flow cessation and after subsequent relaxation at quiescent conditions is shown in Fig. 8c. The hexagonal structure in the gradient-vorticity plane remains unchanged (8c-center). The white strips in $g(r)$ that were observed under shear at $y' = \pm 2.2R\sqrt{3}$ in the $x - y'$ plane are replaced by clear spots (8c-left) and those at $z' = \pm 2.2R$ in the (x, z') plane now contain intense spots at $(x, z') = (0, \pm 2.2R)$ and fainter ones at $(\pm 2R, \pm 2.2R)$ (see Fig. 8c-right). The flowing hexagonal structure of strings thus evolves into a hexagonal crystal after flow cessation.

Concerning orientational order, a first look at the snapshot in Fig. 7c or at the Fig4Blue movie in SI reveals the existence of two regions. In the larger one, outside the red triangle in Fig. 7c, an almost perfect alignment of the director of the platelets along the y' direction is observed after flow cessation. In the smaller region identified by the red triangle, the suspension is crystalline but flow-induced orientational correlations could not relax completely. As a result, the volume-averaged nematic order parameter in the simulation domain is only 0.8 in Fig. 5.

The one-platelet orientation probability at the end of the recovery period now shows a largely dominating peak for angles between 75° and 90°. The secondary peak at 30° that was observed under shear is much smaller and around 40° after flow cessation. More specifically, the two-platelet relative orientations of particles within the same string no longer show the peak at 60° anymore. The preferred orientation is now clearly lower than 10° (see the evolution of curves for spot 2 and 5 between Fig. 9a and 11a). The string locked with OC contacts also survives flow cessation (spots 1 and 4 in the same figure). Platelets belonging to the same string thus share a common orientation vector. The pic-

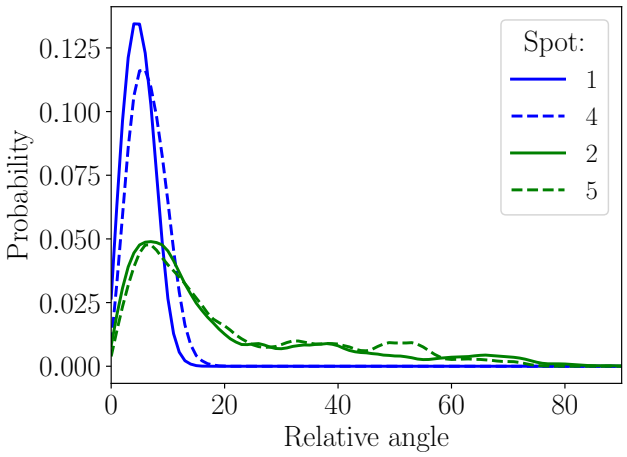

(a) Along one string. Spot numbers are identified in Fig. 8c-left.

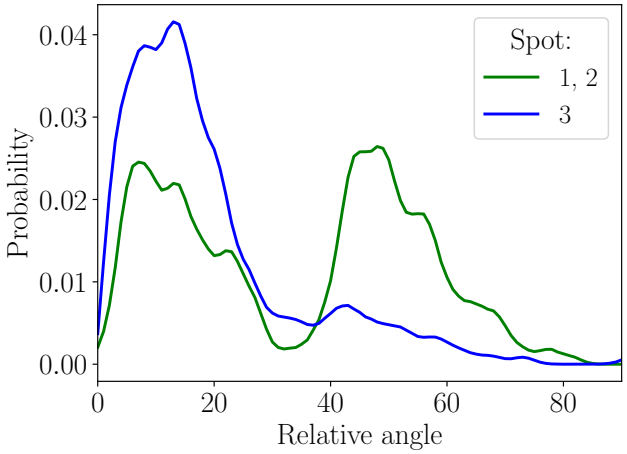

(b) Across different strings. Spot numbers are identified in Fig. 8c-center.

Fig. 11 Probability of relative angles between platelets after flow cessation and relaxation in quiescent conditions ($t/\tau_B = 80$ in Fig. 5).

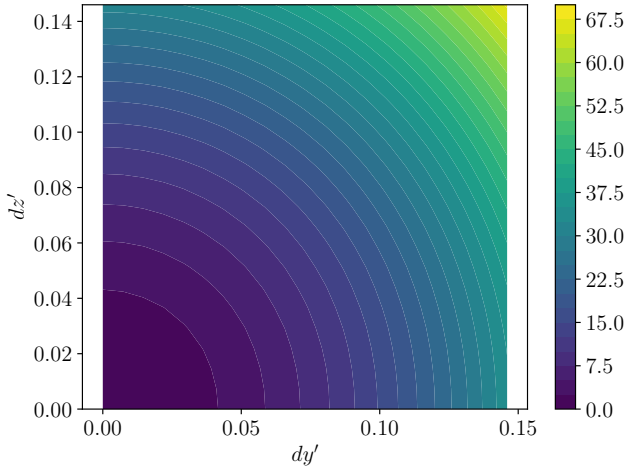

Fig. 12 Interaction energy change ΔV (scaled by kT) for a shift of one platelet in the crystal phase.

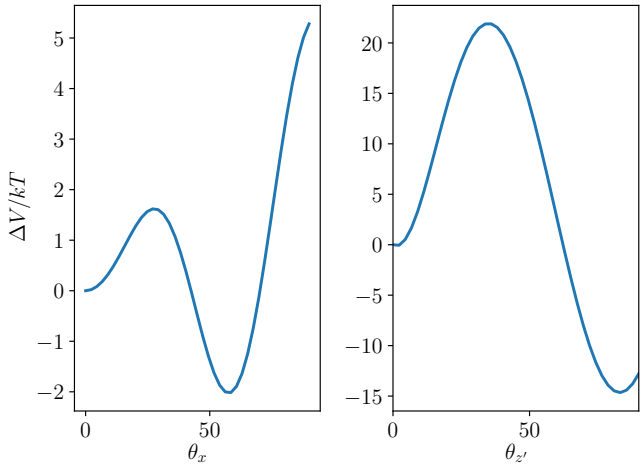

Fig. 13 Energy map for a rotation around x or z' of one platelet in the crystal phase.

ture is slightly more complicated in the gradient-vorticity plane. A relative angle of 10° is slightly preferred overall, after flow cessation, and clearly preferred for spot 3, i.e. for platelets sharing the same plane. There are, however, still a fair number of $50-60°$ relative angles between platelets belonging to different y' planes. They correspond to the small contribution to $P(\theta_x)$ around 40° in Fig. 10, and are associated to the non-nematic region in the red triangle in Fig. 7c.

To our knowledge, obtaining order by relaxation from a flowing system has only been reported by Butera and coworkers[67] for a suspensions of charged colloidal spheres at $\phi = 0.48$. They suspected that this transition was made possible by a certain degree of latent order in the flowing suspension although they could not detect it in their SANS measurements, and thus the mechanism behind the transition was not elucidated. A direct comparison of the present simulations with their results is impossible because our colloidal system is quite different from theirs but, in the following, we will confirm the speculation of the influence of latent order at least qualitatively and give a detailed description of the transition mechanisms for the present anisotropic system.

The evolution of the shear-induced structure after flow cessation can be discussed in the light of the few interaction energy calculations described hereafter. A perfect hexagonal crystalline phase corresponding to the radial distribution function reported in Fig. 8c and with the director of every platelet aligned along y' is now considered as a reference state. The map of the interaction energy change ΔV associated to a shift of the central platelet in directions y' or z' is computed with model (7) and reported in Fig. 12. It confirms that the hexagonal crystalline positional order is indeed an energy minimum.

The effect of a rotation of this platelet either around the x axis or around the z' axis is reported in Fig. 13. Rotations around x show that the perfect nematic state is only a local minimum,

and that a 60° angle of one platelet with respect to a perfectly nematic surrounding is slightly preferred. The energy barrier between these two minima is however less than $2kT$ so one can expect both of them to be encountered. This explains the preferred angles reported in Fig. 11 with two main peaks around 10 and $50-60$ degrees. However, it does not really explain why the nematic order increases after flow cessation. Indeed, the shear flow imposes frequent 60° configurations (Fig. 9 and snapshot 7b) and if they are energy minima the strong increase of nematic order after flow cessation reported in Fig. 5 should not have been observed. The dependence of the energy profile in Fig. 9 to small modifications of the reference state has thus been tested (results not reported here) and they reveal that if one or two neighbours of the central platelet are rotated around x by 60° as would be found at the boundary of the red triangle in Fig. 7c-right, the energy profile of Fig. 13 can show a global minimum at $\theta_x = 0$. This means that it is probably unlikely to have large domains with perfect nematic state. Rather, some defects are necessary to promote alignment in their surrounding. Unfortunately, the size of the simulated domain is not large enough to confirm this speculation. This question deserves further investigation.

Trial rotations around z' show that the perfect nematic state $\theta'_z = 0$ is actually also a local minimum. A platelet with a director close to the x direction ($\theta_{z'} = 90°$) in a crystal with the normal of every other platelet along y' actually involves less energy. It can be understood as the latter configuration involves more face-rim attractions. However, as discussed above, the shear flow tends to first align every platelet with a normal close to y ($\theta_{z'} = 90°$) as shown by the overshoot of S_{nem} in the inset of Fig. 5. Platelets are then largely expected to remain in this local minimum as the energy barrier to escape it is more than $20kT$. The hexagonal crystal with significant nematic order that was obtained after shear is thus actually not an equilibrium structure. It corresponds to a local energy minimum, or arrested state, whose accessibility is determined by the hydrodynamic effects experienced during the shear phase: the hexagonal crystal pattern is imprinted by the hexagonal array of strings due to the flow-induced symmetry breaking, and the cage escape in the initial glassy state is made possible by the application of large hydrodynamic forces at Pe and Ma greater than unity.

At this point it is worth discussing similar structures observed previously. A hexagonal crystal has been mentioned only in the Monte Carlo simulations of Jabbari et al.[35,36] to our knowledge. In their work, platelets are infinitely thin and purely repulsive but it may not be an issue because the glass to crystal transition is obtained in a relatively dilute system with long-range interactions. Their hexagonal crystal is observed around $\kappa D = 2$, which is close to the value of 1.46 used here. In their equilibrium simulations, it appears at dimensionless densities ρ^* above about 6 whereas here $\rho^* = 1$. At lower densities ($\rho^* < 4.5$) they report an isotropic fluid with very large relaxation times, similar to the glassy state considered here as initial condition, and a columnar hexagonal phase with liquid-like order within each column ($4.5 < \rho^* < 6$). So it appears that the application of shear allows a shift of the isotropic to hexagonal crystal transition towards lower densities. The usual mechanistic picture is that shear forces bring energy to the system so platelets can escape the electrostatic cages of the initially isotropic phase. Here, without refuting this idea, it seems that this first results from a hydrodynamic torque that tilts all the platelets in a similar direction, which unlocks translational degrees of freedom.

Note that in their MC simulations Jabbari et al.[35,36] used simulated annealing to remove dependence on initial conditions at the densities leading to the hexagonal crystal. This procedure can also be seen as a means to inject energy in the system in order to escape the initially isotropic phase, but this is in the form of a thermal energy rather than a coherent action like that of shear. Interestingly, we notice the existence of the same hexagonal crystal in the simulations of Jabbari et al. and in the present work although charge anisotropy was not considered in Jabbari's work. It indicates that this anisotropy is not an essential ingredient of the isotropic to crystal transition. This is not totally surprising as the initial state is already defined by the strong, long-range repulsions due to the net charge of the platelets.

Experimentally, a smectic B structure sharing some features with a hexagonal crystal has been observed for gibbsite platelets suspended in DMSO, a solvent allowing very low ionic strengths.[68] In such a structure, hexagonal crystalline order is observed inside smectic layers but no order exists across different layers and the platelet directors are oriented along the normal of the layers. A difference between the present results and the smectic B phase is that here the platelet directors are within the hexagonal layers. Other than that, the physico-chemical conditions investigated in Ref. 68 were quite similar to the present ones: long range repulsive interactions with $\kappa D \simeq 2$ and volume fraction around 0.05. On a side note, these authors imposed an initial prolonged mechanical stirring to the samples in order to verify that the system was not kinetically arrested. Therefore it seems possible that their smectic B phase could be obtained with the help of shear induced ordering as in the present work. The reason why they didn't obtain a 3D crystal as here is unclear. It may be due to unavoidable platelet polydispersity, an important difference between simulations and experiments that would prevent correlation between layers.

A smectic B phase has also been observed in Monte Carlo simulations by Delhorme et al. for similar physico-chemical conditions.[65] In this work, platelets within layers were however locked in OC configuration. This difference is likely to be due to the attractive face-rim interactions present in these simulations and absent in gibbsite systems. In the present work, the small aspect ratio of platelets is thought to be the reason for the absence of charge anisotropy effects during the crystal formation.

To conclude, it has been shown that in the present clay-like model system the sequence of shear and relaxation in quiescent conditions can trigger a glass-to-nematic-crystal transition. This transition is rather complex as is takes place in two distinct stages. First a hexagonal array of flowing strings is formed under shear, with positional order inside each string but no correlations across different strings in the flow direction. Under flow, only partial orientational order is observed. It is only after relaxation in quiescent conditions that the string structure shifts to form a hexagonal crystal and the orientational correlations increase until a nematic

state is obtained.

As mentioned in the introduction, yielding of a suspension has been shown to be a one step process for significantly anisotropic rod-like particles due to the strong translation-rotation coupling.[42–44] In the present system of disk-like particles, positional and orientational degrees of freedom are also strongly coupled. More than just a way to provide energy to the system, the shear flow seems to be the key to ordering by first imposing a strong tumbling motion to every platelet in the suspension (see the peak of S_{nem} in the inset of Fig. 5), which tends to align more or less all platelet directors with the gradient direction and thus to weaken the local disorder thought to be at the origin of the initial arrested state. In this transient partially nematic glassy state, centers of mass can once again rearrange, which leads to the string phase with partial orientational order. As long as the suspension is under flow, no cross-correlation in the x direction can appear between strings flowing at different velocities so the suspension can only crystallize in the gradient-vorticity plane. During the relaxation period, the 3D crystal is sufficiently close to the string phase in terms of energy to be reached with the help of thermal fluctuations, and this completely ordered structure leaves more free volume to each platelet which in turns facilitates rotations to form the nematic state. To summarize, shear first forces partial orientational correlations, which unlocks translational degrees of freedom to obtain a partially ordered structure, and subsequent relaxation in quiescent conditions permits to achieve positional order, which in turn unlocks orientational ordering.

In the next section, the mechanical response of the glassy suspension to the startup shear flow sheds some light on the mechanisms at play during the shear-induced glass-to-crystal transition.

5 Mechanical response of the suspension during shear

The instantaneous mechanical response of the suspension to startup shear and to flow cessation is examined in terms of normal and shear stresses in the next two sections.

5.1 Normal stresses

Let us first consider the one component model (OCM) electrostatic stress defined here as

$$\Sigma_{ij}^{\mathrm{OCM}} = -\frac{1}{V}\sum_{\mathrm{col}} X_{ci}F_{cj}, \tag{13}$$

where V is the volume of the suspension and the sum runs over all platelets. This is not the complete osmotic stress as the ideal part and a contribution from small ions are missing but it gives a good overview of the effect of interparticle forces on the stress evolution during startup shear and the glass-to-crystal transition. The evolution of the OCM pressure defined as $P^{\mathrm{OCM}} = -tr(\mathbf{\Sigma^{OCM}})/3$ is reported in Fig. 14. During the first period without shear flow, a classical transient is observed for the first 10 units of time τ_B, followed by a stationary regime. When shear is applied, the pressure drops significantly in less than one unit of strain and then fluctuates around a constant value during the flow (inset of Fig. 14). Upon flow cessation, the pressure increases again during

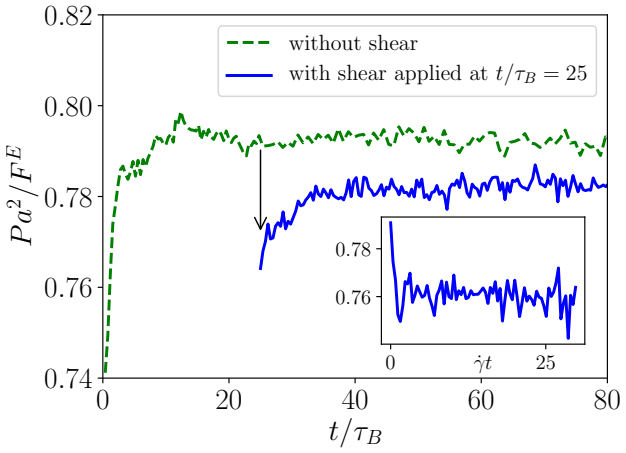

Fig. 14 Evolution of the electrostatic OCM pressure with (blue lines) or without (green dashed lines) shear-induced ordering. Main figure: quiescent conditions. Inset: during shear.

a new transient of about 10 units of time but it settles at a value smaller than the one obtained in the initial glassy state. Koumakis and coworkers already noted a tendency of suspensions to reach a shear-induced structure lowering stresses.[69] This global evolution confirms that shear helped to trigger a transition towards a new state with lower energy, although there is no proof this is a global energy minimum. It also shows that the restructuration under shear happens quite fast, here for a strain of 0.4. This is the deformation required to break one electrostatic cage in this initially positionally isotropic state. Hence the present crystal formation involves a modification of the initial structure only at short distances. An elastic to viscous transition of various deionized clay suspensions, including Laponite, at a small critical strain between 0.07 and 0.4 has already been reported and seems to be a fairly generic feature.[70–72] In an initially nematic Gibbsite suspension in glycerol, Lettinga and coworkers also observed this elastic to viscous transition and associated the elastic response to the tilting of the platelets directors.[73,74]

Forcing a structural transition with shear is somewhat specific as it breaks some symmetries of the initial state, unlike an isotropic compression. Here we can observe that this symmetry breaking is imprinted in the final structure by examining the three normal electrostatic OCM stresses reported in Fig. 15. Before applying shear, these stresses should be isotropic. The weak residual anisotropy remaining at the end of the initial relaxation period is due to the non-perfectly isotropic initial configuration and the non-ergodicity of the suspension. When shear is applied, directions 1, 2, and 3 are no longer equivalent and the flow imposes its own stress anisotropy after a few units of strain (inset of Fig. 15). Indeed, the initially smaller Σ_{22} becomes larger than Σ_{33} during this period of shear. Moreover, the stress anisotropy is enhanced. Interestingly, this anisotropy is enhanced again after flow cessation and remains imprinted in the final relaxed crystal (blue curves in the main figure 15). The absence of relaxation of the suspension towards an isotropic stress state after flow cessa-

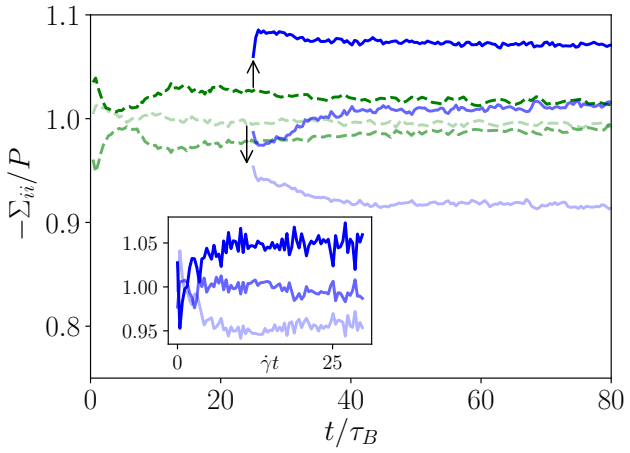

Fig. 15 Evolution of the scaled normal stresses with (blue lines) or without (green dashed lines) shear-induced ordering. Dark green/blue: $-\Sigma_{11}/P$; Normal green/blue: $-\Sigma_{22}/P$; Light green/blue: $-\Sigma_{33}/P$. Main figure: quiescent conditions. Inset: during shear.

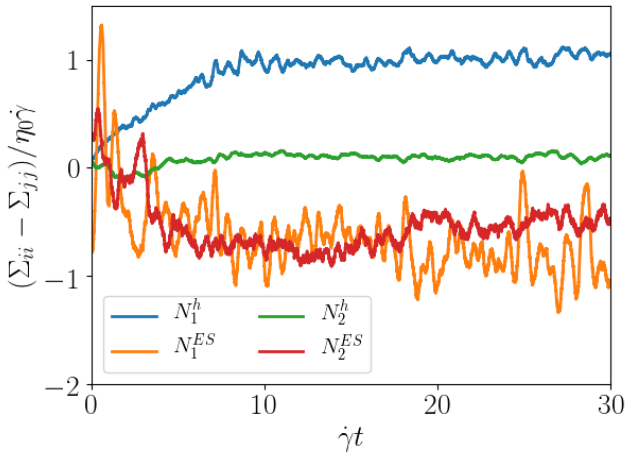

Fig. 16 Evolution of the hydrodynamic (h superscript) and electrostatic (ES superscript) contributions to the first and second normal stress differences during shear. The Brownian component is negligible.

tion means that this suspension possesses a yield stress with an amplitude larger than the residual stress anisotropy.

Further analysis of stress anisotropy is possible by examining the normal stress differences (NSD) $N_1 = \Sigma_{11} - \Sigma_{22}$ and $N_2 = \Sigma_{22} - \Sigma_{33}$ during shear (Fig. 16). During the first unit of strain, the hydrodynamic contribution to N_1 is slightly positive and the electrostatic contribution exhibits a strong positive overshoot. Considering the initial fairly isotropic glassy configuration, the deformation induced by the shear flow is expected to momentarily increase the packing in the y direction after one unit of strain, and as a consequence reduce the packing in the x direction at the same time. As the present system is essentially repulsive, reducing inter-particle distances in the y direction is immediately translated into an increased compression in the y direction. Similarly, the x compression is reduced due to increased average separations in the x direction. This yields a positive electrostatic first normal stress difference. This effect is similar to the Reynolds dilatancy mechanism for hard spheres, but is obtained for soft interactions here. After a few units of strain the string structure is attained and the stress distribution changes again. The dominant compression of electrostatic nature is now in the flow direction (Fig. 15) and it is responsible for the negative electrostatic contribution to N_1 at long times (see Fig. 16). This dominant x-wise compression is believed to be due to the small distances of closest approach between platelets in the x (string) direction that induce important rim-rim repulsions. Since strings are compressed in the x direction, a stabilization mechanism is required to prevent their bending or destruction. The stabilization could be of electrostatic origin, or it could be a hydrodynamic effect. Indeed, the long-time hydrodynamic contribution to N_1 is positive, which could be due to the flow between strings sliding at different velocities. During shear flow, hydrodynamic interactions could stabilize the alignment of the strings along the x direction. However the stability of the crystal after flow cessation, with even increased NSD, seems to indicate that hydrodynamic interactions are not essential for the stabilization of the structure. A side-by-side preferred organization of clay platelets has been discussed by Kleshchanock et al. to explain the formation of the smectic B phase in their experiments.[68] They invoked two hypotheses, namely the lower energy involved in rim-rim interactions compared to face-face interactions, which would promote small distances between rims, and a reduced local screening length between two close rims due to the enhanced counterion concentration there. Due to the electrostatic model employed here, the screening length is imposed and identical throughout the simulation domain so the second hypothesis is ruled out.

The hydrodynamic contribution to N_2 is too close to zero for its sign to be commented, and N_2^{ES} is still evolving at the end of the shear period. So apart from noting that the electrostatic contribution to N_2 is largely dominating, we do not feel much more can be said.

5.2 Shear stress

The time evolution of the shear stress Σ_{12} during the shear period is reported in Fig. 17. It indicates a fairly stable hydrodynamic contribution but a strongly varying electrostatic contribution. The strong overshoot during the first strain unit is associated to the cage breaking event described above. After a transient of about 10 units of strain, the electrostatic contribution to the viscosity is stabilized around a value about half the hydrodynamic contribution for $Ma = 1$. Results not presented here show that the electrostatic contribution dominates only for $Ma < 1$. Strong oscillations are observed at all times, with a period of one strain unit. They correspond to cage hopping events when strings slide one over another.

Two useful quantities characteristic of the mechanical behavior of the suspension can be extracted from the time-dependent shear stress response. At long times, the steady shear relative viscosity

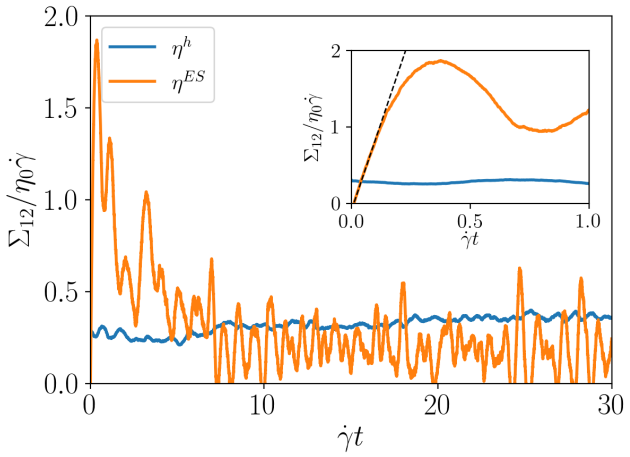

Fig. 17 Evolution of the shear stress during the period of shear.

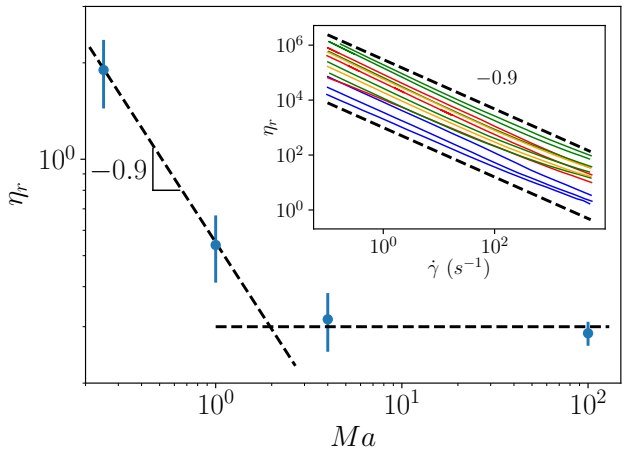

Fig. 18 Steady shear viscosity as a function of Ma. The error bar scale is the standard deviation of the small viscosity oscillations around the average viscosity value (see Fig. 17). ($\kappa D = 1.46, \phi = 0.05$) Inset: experimental results from Fig. 5 of Ref. 72 obtained for different deionized smectite aqueous suspensions and for the largest volume fractions. Following the notations of Ref. 72, blue: SBId-1 S3; red: SAz-1 S2; green: SWy-2 S2; orange: Milos S2.

is obtained as the plateau value of $\Sigma_{12}/\eta_0\dot{\gamma}$. At short times, the shear modulus G' can be measured from the initial slope of Σ_{12} for small deformations (see inset of Fig. 17). The influence of the ratio of hydrodynamic and electrostatic forces Ma on these values is reported in Figs. 18 and 19. Two regimes dominated by electrostatic or hydrodynamic effects can be observed for $Ma < 1$ and $Ma \gg 1$, respectively. For $Ma \gg 1$ the viscosity becomes progressively independent of the value of Ma. This is expected as it corresponds to a situation where the weight of electrostatic forces is negligible compared to the contribution of hydrodynamic interactions. So the viscosity asymptotes towards its value for hard platelet suspensions. For $Ma < 1$, the relative viscosity is well described by the scaling $\eta_r \sim Ma^{-0.9}$. Although this is only based on two points here, such a power law is also observed in the experimental results of Paineau and coworkers[75] for strongly deionized suspensions of different smectite clays at the volume fractions for which a significant yield stress is observed (see inset of Fig. 18). Such a good agreement is interesting, and the power law may be generic, as the aspect ratio of these clays is at least one order of magnitude larger than the one of the present AR7 model platelets.

The shear modulus of the initially glassy suspension is reported in Fig. 19. It is well described by the scaling $G' \sim Ma^{-1}$, which can be rationalized as follows. The suspensions considered here are rather hydrodynamically dilute because the volume fraction is only 0.05 but they are electrostatically very concentrated due to the long range electrostatic interactions. This explains the observation of a hydrodynamic viscosity η^h fairly independent of strain, more precisely of the details of the microstructure, in the insets of Fig. 17 and 19. At short times and for $Ma < O(1)$, the strain-dependent part of the shear stress response is dominated by the electrostatic contribution to the stress η^{ES}, which is independent of $\dot{\gamma}$ and can be expected to scale linearly with strain and equilibrium pressure scale, i.e. as $\gamma F^E/R^2$. Hence in the present

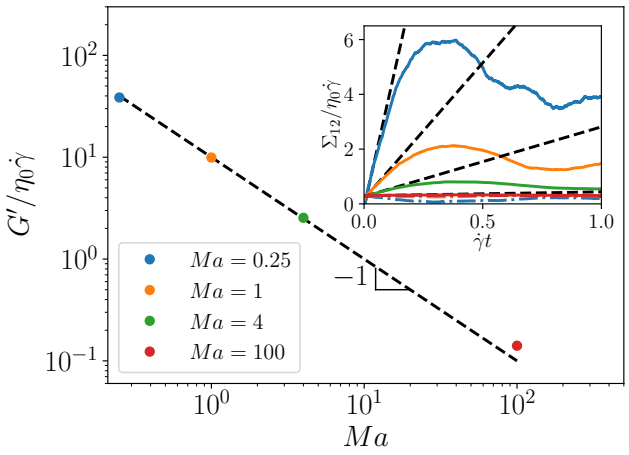

Fig. 19 Shear modulus as a function of Ma. Inset: shear stress as a function of strain at short times (continuous lines) and its hydrodynamic contribution (dot-dashed lines).

glassy suspensions

$$\Sigma_{12}(\dot{\gamma}t \ll 1) \simeq \eta_0^h \dot{\gamma} + \alpha \frac{F^E}{R^2} \dot{\gamma} t \tag{14}$$

where $\eta_0^h \simeq 0.3$ here and α is a constant of order 1. The scaled shear modulus is thus

$$\frac{G'}{\eta_0 \dot{\gamma}} \sim \frac{F^E}{\eta_0 \dot{\gamma} R^2} = Ma^{-1}. \tag{15}$$

The mechanical response of sheared platelet suspensions with long range interactions can then be summarized as follows. For strains smaller than about one, the response of initially glassy suspensions is mainly elastic and associated to the strong repulsive electrostatic interactions. The shear stress and the first normal stress difference both exhibit a positive overshoot due to a first cage breaking event. The scaled shear modulus evolves as Ma^{-1} for $Ma < 1$, confirming the strong prevalence of electrostatic repulsions at short time/strain. After a few units of strain, the hexagonal array of platelet strings is formed and is stable under steady shear. At small Ma, the steady shear viscosity is found to scale as $Ma^{-0.9}$, in line with what can be observed on different smectite clay suspensions. The total normal stress differences under steady shear are too noisy in order to comment on their sign. However, it appears clearly that the hydrodynamic component of N_1 is positive whereas its electrostatic component is negative. The latter indicates the existence of strongly repulsive electrostatic forces between platelets within each string under flow. These forces are likely to be due to the reduced inter-particle distances within one string. As the stress anisotropy is maintained upon flow cessation, the stabilization of strings is also an electrostatic effect. A possible explanation is that a small motion of a platelet in a direction transverse to a string might require too much energy as face-face interactions will be triggered in response to this motion, in contrast to the weaker rim-rim interactions within one string.

6 Conclusions

Relaxed (equilibrium or arrested) states of platelet suspensions and their response to a shear flow have been investigated numerically with Accelerated Stokesian Dynamics. The present platelets were designed as anisotropic model particles with features close to those of clay colloids. The charge anisotropy of platelets has been prescribed carefully with a renormalization procedure enforcing the same reduced temperature as Laponite particles. The phase diagram was consistent with previous works on model clay-like objects and experimental studies on Laponite. A bonded and non-bonded glasses, and different percolated structures including equilibrium gels were observed at intermediate and long ranges of interaction.

When submitted to a shear flow, glassy suspensions are first partially ordered: strings aligned with the flow direction and hexagonally arranged in the gradient-vorticity plane are formed and orientational correlations develop with preferential relative angles of 10° or 60° between platelets. During this shear phase, the mechanical response of the suspension is strongly dominated by electrostatic stresses. Just after the startup of shear, the shear modulus is observed to be proportional to the electrostatic force scale and the shear stress and first normal stress difference both exhibit positive overshoots typical of dense repulsive systems. This transient stage lasts for about one unit of strain and is thus associated to the first cage breaking events. Under steady shear, the relative viscosity of the strings phase is observed to vary as $Ma^{-0.9}$, or $\dot{\gamma}^{-0.9}$, as in experiments performed on various deionized smectite clay suspensions by Paineau and coworkers.[72]

After flow cessation, the shear induced positional order is improved while platelets increase their orientational order. The resulting structure is a hexagonal crystal with smectic orientational order that keeps a memory of the stress anisotropy introduced during the shear period. Moreover, energy calculations show that this final structure does not correspond to a global energy minimum. This is thus a new arrested state with strong order imprinted by the shear flow.

The simulations presented here are among the first ones to permit a simultaneous examination of structure and mechanical response, including the important hydrodynamic response, on the time scale of the glass-to-crystal transition in anisotropic suspensions. They revealed in particular that positional and orientational order are not obtained simultaneously due to shear. Rather, shear first tilts platelets in a more or less common direction, which unlocks translational degrees of freedom. Then, a hexagonal array of strings is formed with strong order along each string but not across different strings. This is a structure that seems to minimize stresses under flow. When the suspension is brought back to rest, positional and orientational correlations evolve again so the structure reaches a local energy minimum. During this relaxation period, shear-induced increased positional correlations are thought to favor the propagation of orientational order throughout the suspension. The glass-to-crystal transition mechanism uncovered here may be quite generic for other colloids with significant geometric anisotropy and that exhibit strong translation-orientation coupling due to long range anisotropic repulsive interactions.

Here we investigated only short time microstructure dynamics to elucidate the mechanisms behind a shear-induced glass-to-crystal transition. If the maximum time scale reachable with Stokesian Dynamics could be increased, an interesting extension to this work would be to examine the influence of hydrodynamics in long time aging and structure-property relationships as recently done experimentally on attraction-driven glasses.[76]

Conflicts of interest

There are no conflicts to declare.

Acknowledgements

We acknowledge the UNITI program chaires d'attractivité 2015 ANR-11-IDEX-0002-02 for general financial support. This work was performed using HPC resources from GENCI-CINES/IDRIS/TGCC (Grants 2019-A0060910109 and 2020-A0080911444).

Notes and references

1 Z.-Y. Li, B.-Y. Gu and G.-Z. Yang, *Physical Review Letters*, 1998, **81**, 2574.

2 M. A. Priolo, D. Gamboa, K. M. Holder and J. C. Grunlan, *Nano letters*, 2010, **10**, 4970–4974.

3 J. D. Forster, J.-G. Park, M. Mittal, H. Noh, C. F. Schreck, C. S. O'Hern, H. Cao, E. M. Furst and E. R. Dufresne, *ACS nano*, 2011, **5**, 6695–6700.

4 A. Van Blaaderen, *Mrs Bulletin*, 2004, **29**, 85–90.

5 J. Vermant and M. J. Solomon, *Journal of Physics: Condensed Matter*, 2005, **17**, R187.

6 S. Mossa, C. De Michele and F. Sciortino, *The Journal of chemical physics*, 2007, **126**, 014905.

7 R. Hoffman, *Transactions of the Society of Rheology*, 1972, **16**, 155–173.

8 J. J. Erpenbeck, *Physical review letters*, 1984, **52**, 1333.

9 B. J. Ackerson, J. B. Hayter, N. A. Clark and L. Cotter, *The Journal of chemical physics*, 1986, **84**, 2344–2349.

10 B. J. Ackerson and P. Pusey, *Physical review letters*, 1988, **61**, 1033.

11 H. Laun, R. Bung, S. Hess, W. Loose, O. Hess, K. Hahn, E. Hädicke, R. Hingmann, F. Schmidt and P. Lindner, *Journal of Rheology*, 1992, **36**, 743–787.

12 S. R. Rastogi, N. J. Wagner and S. R. Lustig, *The Journal of chemical physics*, 1996, **104**, 9234–9248.

13 B. J. Ackerson, *Physica A: Statistical Mechanics and its Applications*, 1991, **174**, 15–30.

14 A. Sierou and J. F. Brady, *Journal of Rheology (1978-present)*, 2002, **46**, 1031–1056.

15 A. M. Leshansky and J. F. Brady, *Journal of Fluid Mechanics*, 2005, **527**, 141.

16 S. D. Kulkarni and J. F. Morris, *Journal of Rheology*, 2009, **53**, 417–439.

17 B. J. Ackerson, *Journal of Rheology*, 1990, **34**, 553–590.

18 J. Vermant, L. Raynaud, J. Mewis, B. Ernst and G. Fuller, *Journal of colloid and interface science*, 1999, **211**, 221–229.

19 M. Haw, W. Poon and P. Pusey, *Physical Review E*, 1998, **57**, 6859.

20 N. Koumakis, A. Schofield and G. Petekidis, *Soft Matter*, 2008, **4**,.

21 T. Besseling, M. Hermes, A. Fortini, M. Dijkstra, A. Imhof and A. Van Blaaderen, *Soft Matter*, 2012, **8**, 6931–6939.

22 F. Khabaz, M. Cloitre and R. T. Bonnecaze, *Physical Review Fluids*, 2018, **3**, 033301.

23 S. Paulin, B. J. Ackerson and M. Wolfe, *Journal of colloid and interface science*, 1996, **178**, 251–262.

24 J.-R. Huang and T. Mason, *EPL (Europhysics Letters)*, 2008, **83**, 28004.

25 J.-R. Huang and T. G. Mason, *Soft Matter*, 2009, **5**, 2208–2214.

26 J. Ruiz-Franco, J. Marakis, N. Gnan, J. Kohlbrecher, M. Gauthier, M. P. Lettinga, D. Vlassopoulos and E. Zaccarelli, *Phys. Rev. Lett.*, 2018, **120**, 078003.

27 B. Ackerson and N. Clark, *Physical Review A*, 1984, **30**, 906.

28 Y. Yan and J. Dhont, *Physica A: Statistical Mechanics and its Applications*, 1993, **198**, 78–107.

29 S. R. Rastogi, N. J. Wagner and S. R. Lustig, *The Journal of chemical physics*, 1996, **104**, 9234–9248.

30 F. Khabaz, T. Liu, M. Cloitre and R. T. Bonnecaze, *Physical Review Fluids*, 2017, **2**, 093301.

31 Z. Zhang and S. C. Glotzer, *Nano letters*, 2004, **4**, 1407–1413.

32 E. Bianchi, J. Largo, P. Tartaglia, E. Zaccarelli and F. Sciortino, *Physical review letters*, 2006, **97**, 168301.

33 S. C. Glotzer and M. J. Solomon, *Nature materials*, 2007, **6**, 557–562.

34 F. Chu, M. Siebenbürger, F. Polzer, C. Stolze, J. Kaiser, M. Hoffmann, N. Heptner, J. Dzubiella, M. Drechsler, Y. Lu *et al.*, *Macromolecular rapid communications*, 2012, **33**, 1042–1048.

35 S. Jabbari-Farouji, J.-J. Weis, P. Davidson, P. Levitz and E. Trizac, *Scientific Reports*, 2013, **3**, 3559.

36 S. Jabbari-Farouji, J.-J. Weis, P. Davidson, P. Levitz and E. Trizac, *The Journal of Chemical Physics*, 2014, **141**, 224510.

37 E. Grelet, *Physical Review X*, 2014, **4**, 021053.

38 B. Liu, T. H. Besseling, A. van Blaaderen and A. Imhof, *Physical review letters*, 2015, **115**, 078301.

39 F. Chu, N. Heptner, Y. Lu, M. Siebenbürger, P. Lindner, J. Dzubiella and M. Ballauff, *Langmuir*, 2015, **31**, 5992–6000.

40 E. Mock and C. Zukoski, *Journal of Rheology*, 2007, **51**, 541–559.

41 R. Zhang and K. S. Schweizer, *Physical Review E*, 2009, **80**, 011502.

42 R. Zhang and K. S. Schweizer, *The Journal of chemical physics*, 2010, **133**, 104902.

43 R. C. Kramb and C. F. Zukoski, *Journal of Rheology*, 2011, **55**, 1069–1084.

44 R. C. Kramb and C. F. Zukoski, *Journal of Physics: Condensed Matter*, 2010, **23**, 035102.

45 A. Sierou and J. F. Brady, *Journal of Fluid Mechanics*, 2001, **448**, 115–146.

46 A. J. Banchio and J. F. Brady, *The Journal of Chemical Physics*, 2003, **118**, 10323–10332.

47 S. Kim and S. J. Karrila, *Microhydrodynamics: principles and selected applications*, Courier Corporation, 2013.

48 Q. Meng and J. J. Higdon, *Journal of Rheology*, 2008, **52**, 1–36.

49 Q. Meng and J. J. Higdon, *Journal of Rheology*, 2008, **52**, 37–65.

50 J. W. Swan, J. F. Brady, R. S. Moore and C. 174, *Physics of Fluids*, 2011, **23**, 071901.

51 V. Labalette, *PhD thesis*, Université de Toulouse, Institut National Polytechnique de Toulouse, 2020.

52 H. Kawabata, D. Nishiura, H. Sakaguchi and Y. Tatsumi, *Rheologica Acta*, 2013, **52**, 1–21.

53 S. Alexander, P. M. Chaikin, P. Grant, G. J. Morales, P. Pincus and D. Hone, *J. Chem. Phys.*, 1984, **80**, 5776–5781.

54 E. Trizac, L. Bocquet, M. Aubouy and H. H. von Grünberg, *Langmuir*, 2003, **19**, 4027–4033.

55 A. R. Denton, *J. Phys.: Condens. Matter*, 2010, **22**, 364108.

56 N. Boon, G. I. Guerrero-García, R. van Roij and M. O. de la Cruz, *Proc Natl Acad Sci U S A*, 2015, **112**, 9242–9246.

57 Y. Hallez and M. Meireles, *Langmuir*, 2017, **33**, 10051–10060.

58 Y. Hallez and M. Meireles, *The European Physical Journal E*, 2018, **41**, 69.

59 Y. Hallez, J. Diatta and M. Meireles, *Langmuir*, 2014, **30**, 6721–6729.

60 Y. Hallez and M. Meireles, *Langmuir*, 2016, **32**, 10430–10444.

61 L. Teulon, Y. Hallez, S. Raffy, F. Guerin, E. Palleau and L. Ressier, *The Journal of Physical Chemistry C*, 2019, **123**, 783–790.

62 E. Zaccarelli and W. C. Poon, *Proceedings of the National Academy of Sciences*, 2009, **106**, 15203–15208.

63 B. Jonsson, C. Labbez and B. Cabane, *Langmuir*, 2008, **24**, 11406–11413.

64 B. Ruzicka, E. Zaccarelli, L. Zulian, R. Angelini, M. Sztucki, A. Moussaïd, T. Narayanan and F. Sciortino, *Nature materials*, 2011, **10**, 56–60.

65 M. Delhorme, B. Jönsson and C. Labbez, *Soft Matter*, 2012, **8**, 9691–9704.

66 M. Delhorme, C. Labbez and B. Jönsson, *The journal of physical chemistry letters*, 2012, **3**, 1315–1320.

67 R. J. Butera, M. S. Wolfe, J. Bender and N. J. Wagner, *Physical review letters*, 1996, **77**, 2117.

68 D. Kleshchanok, P. Holmqvist, J.-M. Meijer and H. N. Lekkerkerker, *Journal of the American Chemical Society*, 2012, **134**, 5985–5990.

69 N. Koumakis, J. F. Brady and G. Petekidis, *Journal of Non-Newtonian Fluid Mechanics*, 2016, **233**, 119–132.

70 J. Ramsay, *Journal of Colloid and Interface Science*, 1986, **109**, 441–447.

71 A. J. Ten Brinke, L. Bailey, H. N. Lekkerkerker and G. C. Maitland, *Soft Matter*, 2007, **3**, 1145–1162.

72 E. Paineau, I. Bihannic, C. Baravian, A.-M. Philippe, P. Davidson, P. Levitz, S. S. Funari, C. Rochas and L. J. Michot, *Langmuir*, 2011, **27**, 5562–5573.

73 M. Lettinga, P. Holmqvist, P. Ballesta, S. Rogers, D. Kleshchanok and B. Struth, *Physical review letters*, 2012, **109**, 246001.

74 O. Korculanin, D. Hermida-Merino, H. Hirsemann, B. Struth, S. Rogers and M. Lettinga, *Physics of Fluids*, 2017, **29**, 023102.

75 E. Paineau, L. J. Michot, I. Bihannic and C. Baravian, *Langmuir*, 2011, **27**, 7806–7819.

76 M. B. Gordon, C. J. Kloxin and N. J. Wagner, *Soft Matter*, 2021.